Publications of the Astronomical Society of the Pacific, 135:028001 (14pp), 2023 February https://doi.org/10.1088/1538-3873/acac53

Performance of NIRCam on JWST in Flight

Marcia J. Rieke[1], Douglas M. Kelly[1], Karl Misselt[1], John Stansberry[2], Martha Boyer[2], Thomas Beatty[3], Eiichi Egami[1], Michael Florian[1], Thomas P. Greene[4], Kevin Hainline[1], Jarron Leisenring[1], Thomas Roellig[4], Everett Schlawin[1], Fengwu Sun[1], Lee Tinnin[1], Christina C. Williams[5], Christopher N. A. Willmer[1], Debra Wilson[1], Charles R. Clark[6], Scott Rohrbach[6], Brian Brooks[2], Alicia Canipe[2], Matteo Correnti[7,8], Audrey DiFelice[2], Mario Gennaro[2], Julian Girard[2], George Hartig[2], Bryan Hilbert[2], Anton M. Koekemoer[2], Nikolay K. Nikolov[2], Norbert Pirzkal[2], Armin Rest[2,9], Massimo Robberto[2,10], Ben Sunnquist[2], Randal Telfer[2], Chi Rai Wu[2], Malcolm Ferry[11], Dan Lewis[11], Stefi Baum[12], Charles Beichman[13], René Doyon[14], Alan Dressler[15], Daniel J. Eisenstein[16], Laura Ferrarese[17], Klaus Hodapp[18], Scott Horner[19], Daniel T. Jaffe[20], Doug Johnstone[17,21], John Krist[22], Peter Martin[23], Donald W. McCarthy[1], Michael Meyer[24], George H. Rieke[1], John Trauger[22], and Erick T. Young[25]

[1] Steward Observatory, University of Arizona, 933 N. Cherry Avenue, Tucson, AZ 85721, USA; mrieke@arizona.edu
[2] Space Telescope Science Institute, 3700 San Martin Drive, Baltimore, MD 21218, USA
[3] Department of Astronomy, University of Wisconsin, Madison, Madison, WI 53706, USA
[4] NASA Ames Research Center, Space Science and Astrobiology Division, MS 245-6, Moffett Field, CA 94035, USA
[5] National Optical-Infrared Research Laboratory, 950 N Cherry Avenue, Tucson, AZ 85719, USA
[6] Goddard Space Flight Center, Greenbelt, MD, USA
[7] INAF, Osservatorio Astronomico di Roma, via Frascati 33, I-00078, Monteporzio Catone, Rome, Italy
[8] ASI-Space Science Data Center, Via del Politecnico, I-00133, Rome, Italy
[9] Department of Physics and Astronomy, Johns Hopkins University, Baltimore, MD 21218, USA
[10] Johns Hopkins University, 3400 N. Charles Street, Baltimore, MD 21218, USA
[11] Lockheed Martin Advanced Technology Center, 3251 Hanover Street, Palo Alto, CA 94304, USA
[12] Faculty of Science, 230 Machray Hall, 186 Dysart Road, University of Manitoba, Winnipeg, MB R3T 2N2, Canada
[13] NASA Exoplanet Science Institute/IPAC, Jet Propulsion Laboratory, California Institute of Technology, 1200 E California Blvd, Pasadena, CA 91125, USA
[14] Département de physique, Université de Montréal, C.P. 6128, Succursale Centre-Ville, Montréal, QC H3C 3J7, Canada
[15] The Observatories, The Carnegie Institution for Science, 813 Santa Barbara Street, Pasadena, CA 91101, USA
[16] Center for Astrophysics, Harvard & Smithsonian, 60 Garden Street, Cambridge, MA 02138, USA
[17] National Research Council Canada, Herzberg Astronomy and Astrophysics, 5071 West Saanich Rd., Victoria, BC, V9E 2E7, Canada
[18] Institute for Astronomy, 640 N Aohoku Pl Hilo, HI 96720, USA
[19] 881 Spinosa Drive, Sunnyvale, CA 94087, USA
[20] The University of Texas at Austin, Department of Astronomy RLM 16.342, Austin, TX 78712, USA
[21] Department of Physics and Astronomy, University of Victoria, Victoria, BC, V8P 5C2, Canada
[22] Jet Propulsion Laboratory, 4800 Oak Grove Drive M/S 183-900, Pasadena, CA 91109, USA
[23] Canadian Institute for Theoretical Astrophysics, University of Toronto, McLennan Physical Laboratories, 60 St. George Street, Toronto, Ontario, M5S 3H8, Canada
[24] Department of Astronomy, University of Michigan, 1085 S. University, Ann Arbor, MI 48109, USA
[25] USRA, Mountain View, CA, USA
Received 2022 November 15; accepted 2022 December 16; published 2023 February 13

Abstract

The Near Infrared Camera for the James Webb Space Telescope (JWST) is delivering the imagery that astronomers have hoped for ever since JWST was proposed back in the 1990s. In the Commissioning Period that extended from right after launch to early 2022 July, NIRCam has been subjected to a number of performance tests and operational checks. The camera is exceeding prelaunch expectations in virtually all areas, with very few surprises discovered in flight. NIRCam also delivered the imagery needed by the Wavefront Sensing Team for use in aligning the telescope mirror segments.

Unified Astronomy Thesaurus concepts: Infrared telescopes (794); Space observatories (1543); Space telescopes (1547)

1. Introduction

All of the original concepts for what we now call the James Webb Space Telescope (JWST) included a relatively large field-of-view camera spanning at least the 1–5 μm range. NIRCam's science role was initially focused on deep surveys to find the most distant galaxies (Stockman 1997), and of course,

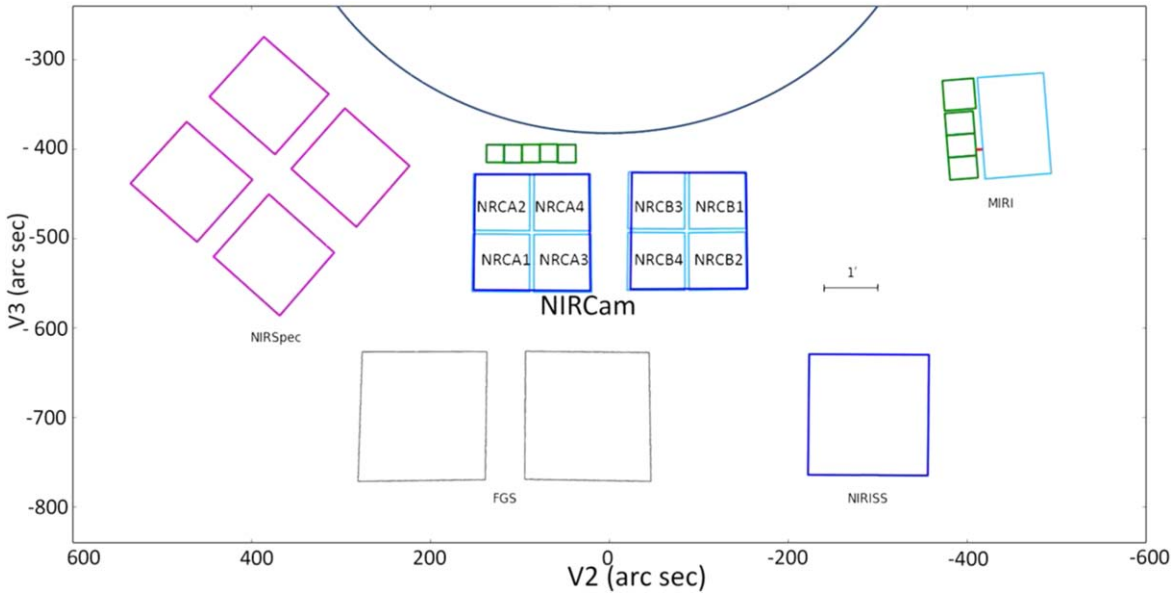

Figure 1. NIRCam's location in the JWST field of view. Designations for the short-wavelength arrays are shown with the long-wavelength arrays called NRCALONG and NRCBLONG with the fields of view outlined in blue. The long-wavelength arrays cover the same area as the four short-wavelength arrays in a module. The small green squares show the locations of the coronagraphic fields. V2 and V3 refer to the telescope coordinate system where V3 points away from the sun shield, and V2 is perpendicular to V3 to form a right-handed coordinate system.

an instrument capable of finding these galaxies is also capable of many other observations. The deep survey use drove the need for as large a field of view as possible since no one knew how common galaxies at $z > 10$ would be at the time NIRCam was being designed. What was known is that photometric redshifts would be a powerful tool, and so NIRCam would need a filter set that spanned its entire wavelength range, with filter widths that needed to be optimized between sensitivity and wavelength discrimination.

Over time, the role of NIRCam expanded to include providing the imaging used for wave-front sensing and telescope alignment, which rendered NIRCam a mission-critical element. The final NIRCam design incorporates two copies (modules) of the camera to provide full block redundancy to maximize the availability of the wave-front-sensing capability. The use of NIRCam as the wave-front sensor also meant that NIRCam must have a very small intrinsic wave-front error so it does not imprint errors on the other instruments (Acton et al. 2004, 2018).

In the final NIRCam design, two modules provide $2\farcm2 \times 2\farcm2$ fields of view, each as shown in Figure 1. Each field of view can be observed using two filters simultaneously through the use of dichroics that split the wavelength range into 0.6 to 2.3 μm and 2.4 to 5 μm with a deadband from 2.3 to 2.4 μm, effectively doubling the field for programs needing full filter coverage. NIRCam also includes components to enable coronagraphy; these do not affect the area available for direct imaging. Grisms in the long-wavelength arms, originally included to expand the coarse phasing capture range, can be used to provide a time-series spectroscopic capability useful for exoplanet observations and to provide wide-field spectroscopy, a powerful tool for finding emission-line galaxies.

Lockheed Martin's Advanced Technology Center led the design and construction of NIRCam. The University of Arizona Team developed the focal-plane assemblies in collaboration with Teledyne Imaging Systems. Arizona also developed the initial pipeline and reference files that were used by Space Telescope Science Institute in producing the first flight pipeline. The Space Telescope Science Institute maintains documentation about the telescope and instruments including NIRCam at https://jwst-docs.stsci.edu/.

2. Design and Construction

The NIRCam design was driven by wanting a large field of view for efficient surveys and by the wave-front error requirement imposed by its use as the mission wave-front sensor. NIRCam is required to have less than 90 nm of absolute wave-front error at 2.12 μm. The ground-to-flight change in the wave-front error is required to be less than 40 nm (Huff 2005). The redundancy imposed by NIRCam being the wave-front sensor meshes well with efficient survey needs since having two complete copies of NIRCam doubles the field of view. Assembly and testing of the two modules were facilitated by including a tip-tilt focus mechanism in each module. This mechanism can be used to align the NIRCam pupil with the telescope as required for wave-front sensing and the coarse

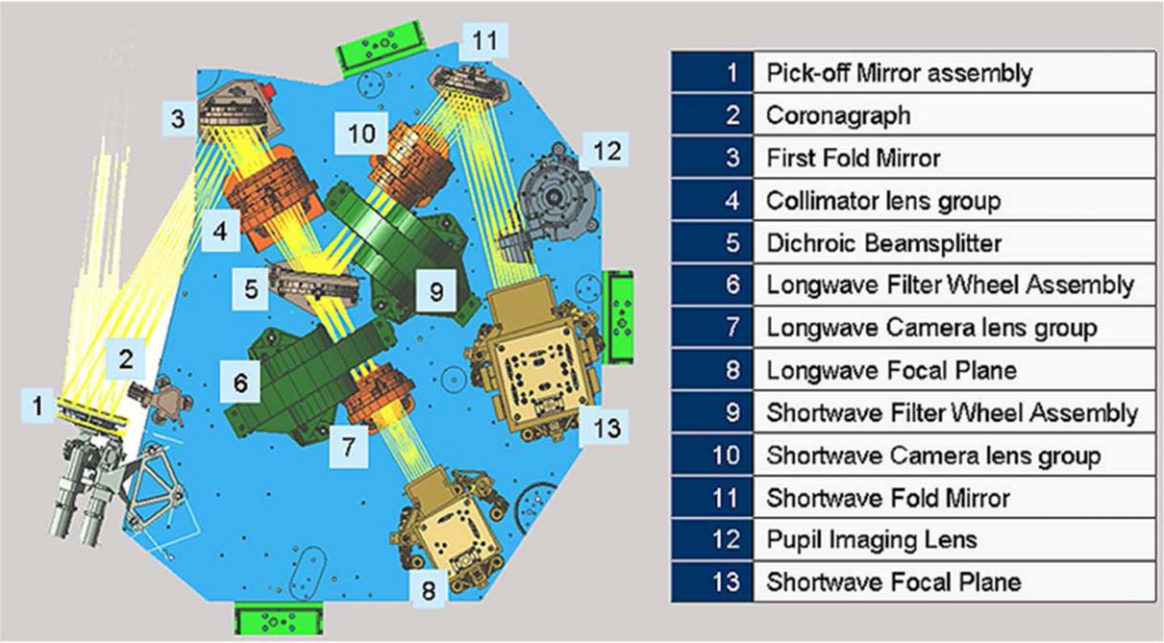

Figure 2. One-half of NIRCam showing its optical train and mechanisms. Starlight from the telescope enters the instrument from the upper left, enters the module after reflection from the pick-off mirror (1) and then reflects into the main body of the camera where the dichroic beamsplitter (5) separates the long- and short-wavelength light. The other module is a mirror image of the one shown here, mounted back to back behind what is shown.

phasing step of aligning the telescope. The ability to adjust the focus of each module separately relaxed the need for each module to have precisely the same focus. The fields of view of the two modules are separated by ∼44″ and cover a total of 9.7 arcmin^2 for one wavelength.

Survey use drove the choice of using dichroics to split the light into short- and long-wavelength optical trains in each of the redundant NIRCam modules. Figure 2 presents the light path and layout of one module. Note that this figure shows the pupil imaging lens in the deployed position rather than the usual retracted position. The wavelength split also facilitates the matching of pixel scales to diffraction-limited sampling so NIRCam provides Nyquist sampling of the point-spread function (PSF) at 2 and at 4 μm. The overlap between the short-wavelength and long-wavelength fields of view is ∼96% in both modules. Each arm in a module has two wheel mechanisms mounted together, with one wheel carrying mainly filters and the other wheel carrying optical elements that need to be used at a pupil as well as some additional filters. The wheels are referred to as the filter wheel and the pupil wheel. They are moved independently.

Another benefit of the short-wavelength/long-wavelength split is that detector arrays (referred to as SCAs for Sensor Chip Assemblies) with different cutoff wavelengths and different antireflection coatings could be used. Teledyne Imaging Systems fabricated the arrays for NIRCam. NIRCam uses eight 2.5 μm cutoff SCAs and two 5 μm cutoff SCAs. It is somewhat easier to make the 2.5 μm devices than the 5 μm devices so the wavelength split eased the production process for this relatively large number of arrays. Finally, the wavelength split also eased the blocking requirements on NIRCam's bandpass filters. The short-wavelength filters do not need blocking beyond the response band of the 2.5 μm detectors. The dichroics have silicon substrates so the long-wavelength filters do not need blocking below 1.08 μm.

A key design choice for NIRCam was the decision to use a refractive design. This choice was motivated by such a design yielding a more compact and less massive instrument. Some of the very early designs for NIRCam using reflective optics yielded an instrument so large that there may not have been room and mass for a fourth instrument on JWST. The refractive design choice also helped enable the fully redundant design.

3. Wave-front Sensing

The JWST primary mirror has eighteen fully adjustable hexagonal segments that must be aligned to perform like a single, monolithic mirror. NIRCam was used to locate all of the segment images after launch and provided the imagery for the initial mirror alignment. The first step in phasing the 18 segments after segment-level adjustments was completed using dispersed Hartmann sensors (DHSs) mounted in the short-wavelength pupil wheel to provide spectra at $R \sim 300$ resulting from the interference of two mirror segments. The F150W2 filter includes two notches in its spectral response shown in

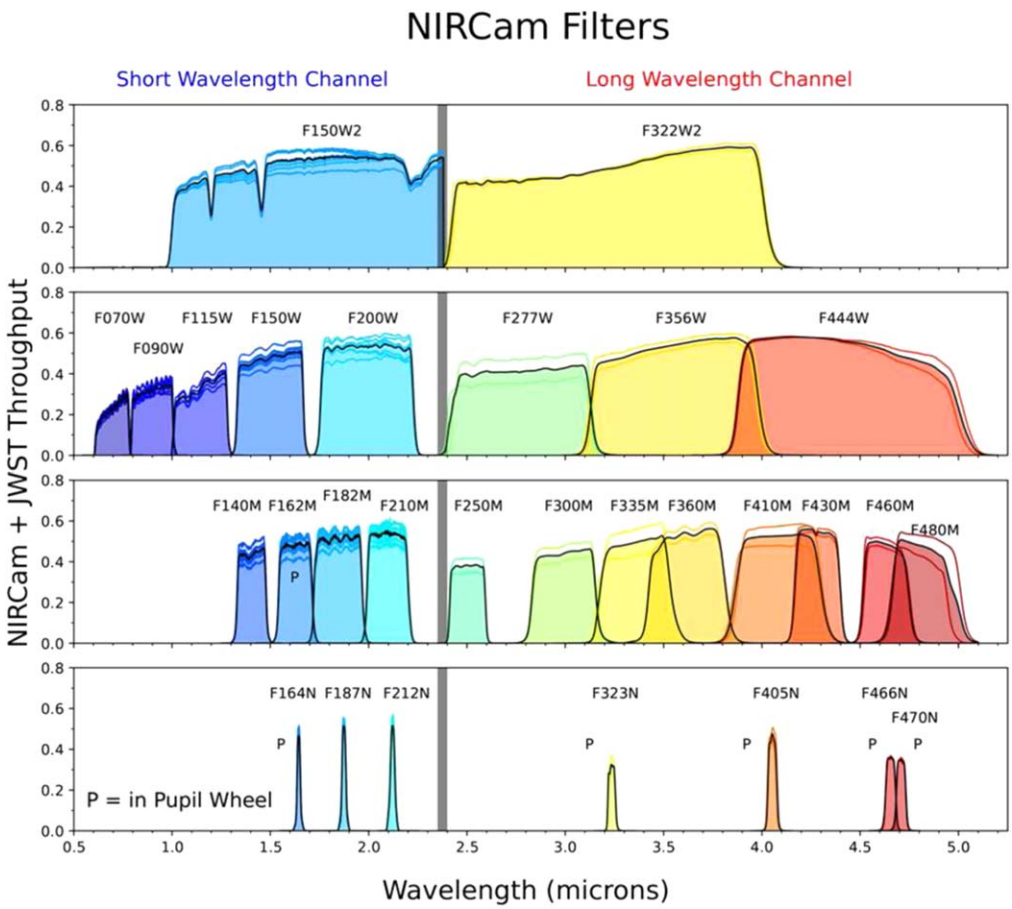

Figure 3. Throughputs of NIRCam's filters. All terms affecting throughput including detector quantum efficiency and telescope reflectivity are included. The gray bar denotes the dichroic deadband. The letter "P" indicates filters that are mounted on the pupil wheels.

Figure 3, which provides the wavelength calibration needed to convert the interference pattern into a piston difference between the segments. Each DHS spans 10 segment pairs and produces 10 spectra. The two DHSs are mounted at 60° with respect to each other to provide 20 separate measurements to adjust the segments in piston. Relatively large focus steps between segments can be measured using these data, and were a key step in the initial mirror alignment but not needed for routine wave-front sensing.

Every 2 days, NIRCam takes images for focus diverse phase retrieval to monitor the alignment of the primary mirror. Mirror adjustments are then executed when the alignment has drifted to where the overall observatory wave-front error has increased to ∼80 nm. These adjustments have been needed on average about every 17 days. Focus diversity is achieved by using weak lenses in the short-wavelength arm with one mounted in the filter wheel and two in the pupil wheel. These lenses defocus the starlight by either ±4 waves, ±8 waves, and as much as +12 waves using +4 and +8 in series. The wave-front sensing is executed at a wavelength of 2.1 μm. Two of these weak lenses, +4 and +8, can also be used to defocus stars observed in time-series measurements (see Section 4.4). Focus diverse phase retrieval and the overall wave-front sensing process are described in detail in Acton et al. (2012, 2022) and Perrin et al. (2016).

4. Observing Modes

NIRCam has five observing modes. Two of these modes, the grism time series and photometric time series, are very similar. Table 1 presents the basic characteristics of the modes. The imaging mode serves as the basis for all five modes with its collection of data from both short-wavelength and long-wavelength arms simultaneously and with detectors read out using sampling up the ramp. The wide-field slitless spectroscopic (WFSS) mode includes the acquisition of direct images in addition to the grism images to enable source detection and wavelength calibration in the spectroscopic images. In this mode, the short-wavelength arm is used for direct imaging. For the grism time series, the long-wavelength arm uses a grism in series with a bandpass filter for out-of-band blocking. The

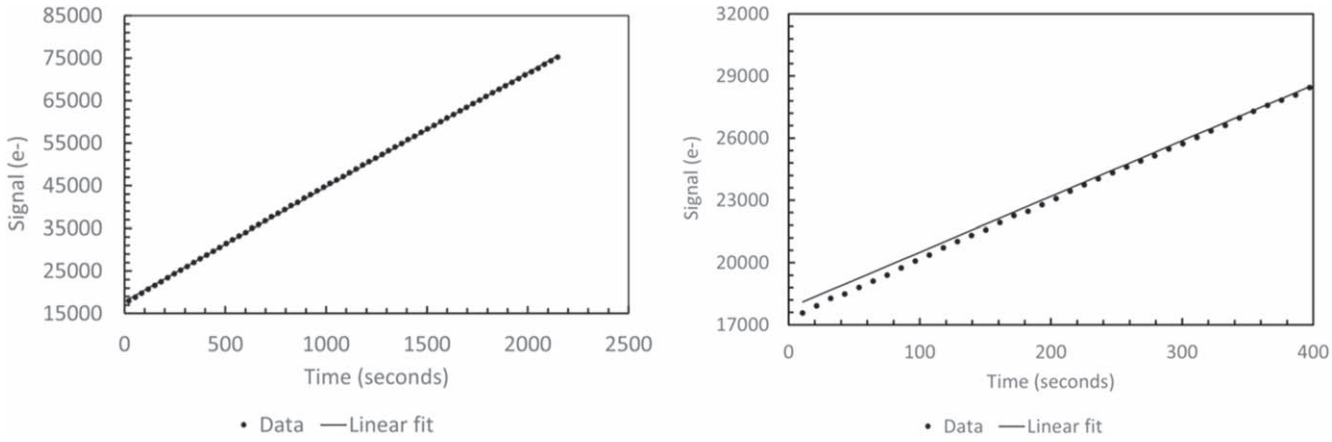

Figure 4. On the left, a ramp for a pixel illuminated by a star showing the linear behavior of the charge collection. On the right, the low-signal portion of the ramp illustrates the nonlinearity present at low signal levels.

Table 1
NIRCam Observing Modes

Mode	Number of SCAs Used	Typical Use	Special Requirements
Imaging	2, 5, or 10	General 0.7–5 μm imaging	Subarrays available, RAPID mode using 10 SCAs only for single exposures
WFSS	10 (2 for spectra, 8 for imaging)	Wide-field emission-line survey 2.4–5 μm with short-wavelength imaging	Careful planning needed for full spatial coverage
Grism Time Series	2 (Mod A only)	Transit spectroscopy 2.4–5 μm	Stripe mode can extend bright limit, target acquisition may be desirable
Photometric Time Series	2 or 5 (Mod B only)	High-time-resolution photometry	
Coronagraphy	2 (Mod A only)	High contrast imaging	Target acquisition required

short-wavelength arm is used with a choice of weak lens and the appropriate $\sim$2 μm filter. The photometric time-series mode uses bandpass filters in Module B. In coronagraphic mode, a target star is placed behind an occulter, and images are acquired.

4.1. Imaging Mode

As described earlier, NIRCam's basic imaging mode is used for both science imaging and wave-front sensing imaging. Both short-wavelength and long-wavelength arms are read out simultaneously, but if a point source or limited area is to be observed, only one module of NIRCam can be used to save on data volume. For surveys, both modules can be used. There is no hardware requirement that the two modules be configured with the same filter choices although the Astronomer's Proposal Tool does not support different filters currently. The modules are constrained to use the same readout patterns. If a bright source is observed, subarrays can be used to extend the camera's dynamic range but all arrays must be read out using the same size subarray, so typically only one short-wavelength array and the corresponding long-wavelength array will be read out. In the case of extended bright sources, one long-wavelength and a set of four short-wavelength subarrays at the center of the B module, with approximately overlapping areas, are used. For point sources, one short-wavelength and one long-wavelength subarray can be configured, located at the upper-left corner of the NRCB1, a short-wavelength SCA. Figure 1 shows the location of NIRCam and its SCAs in the JWST focal plane.

The throughput of the telescope plus NIRCam system is higher than prelaunch predictions. This improvement is partly the result of arriving at L2 with fewer particulates and other contaminants such as ice and partly the result of conservatism in the prelaunch estimates. Figure 3 shows the throughputs that are remarkable for a camera employing six lenses, a tribute to the quality of the lens antireflection coatings. The throughput has been measured by comparing the known flux of calibration stars to the detected flux in a 2.″5 radius aperture. The detected flux was corrected to the total flux using an encircled energy curve based on a PSF computed using the optical path difference map for the date of the observation available from the data archive MAST. No correction was made for gaps or strut obscuration in the telescope throughput.

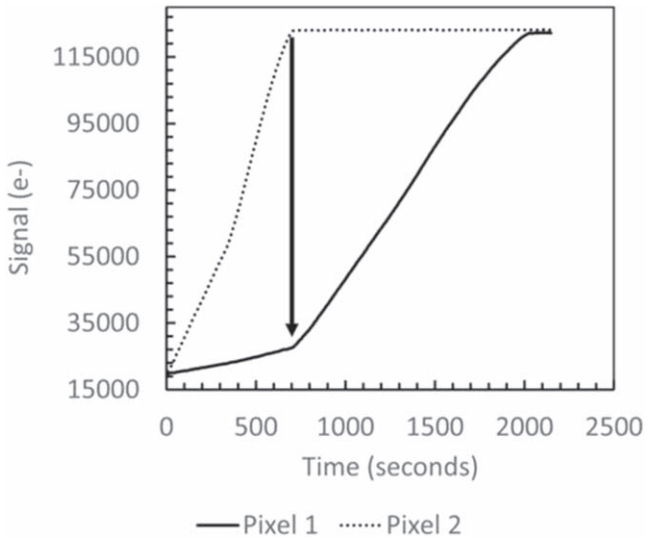

Figure 5. Ramps from adjacent pixels illustrating how the slope changes when the adjacent pixel saturates and charge migration begins.

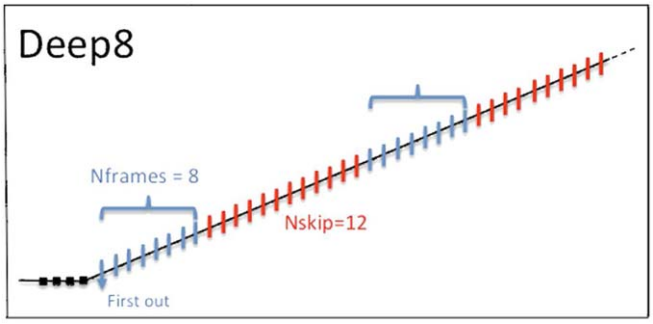

Figure 6. The DEEP8 readout pattern illustrating the coaddition of eight samples and skipping of reads to minimize data volume.

Table 2
NIRCam Sensitivity 10σ in 10,000 s in a 2.5 pixel Radius Aperture with a Background 1.2× the Minimum Zodiacal Light Level

Filter	λ_{pivot} (μm)	(nJy)	Filter	λ_{pivot} (μm)	(nJy)
F070W	0.704	11.85	F277W	2.786	10.59
F090W	0.901	9.74	F356W	3.563	8.88
F115W	1.154	8.57	F444W	4.421	17.31
F150W	1.501	6.99	F250M	2.503	24.63
F200W	1.990	6.22	F300M	2.996	16.75
F140M	1.404	11.85	F335M	3.365	14.91
F162M	1.626	11.35	F360M	3.621	15.14
F182M	1.845	9.28	F410M	4.092	18.74
F210M	2.093	11.56	F430M	4.280	35.14
F164N	1.644	69.08	F460M	4.624	56.81
F187N	1.874	65.00	F480M	4.834	63.75
F212N	2.120	70.31	F323N	3.237	113.73
F405N	4.055	103.44	F466N	4.654	173.14
F470N	4.707	199.80			

Figure 4 displays a pixel ramp from data taken during a Cycle 1 calibration program, illustrating how charge builds up over time from a source and is very linear. The start of the ramp lies below the linear fit, which is indicative of charge being lost to traps in the detector material. This loss of charge to traps could affect low-signal observations but in many cases, there is sufficient charge collection from the zodiacal background that this is not an issue. Figure 5 displays a ramp that reaches saturation and also shows how a pixel that reaches saturation affects the slope of an adjacent pixel as charge migrates from the saturated pixel to adjacent pixels. The migration of saturated charge is mainly a bright object problem but can complicate the extraction of faint sources on the fringes of a bright PSF. The pipeline includes a saturation check and a linearity correction step to compensate for the change in gain of the readout circuit as the charge on the integrating node increases (see Plazas et al. 2017).

NIRCam is background limited through wide filters as predicted before launch. Table 2 gives the current sensitivity for long exposures. The performance of NIRCam's detectors varies somewhat from SCA to SCA. Here we will use instrument-wide averages unless denoted otherwise. The flight read noise and dark current of the NIRCam short-wavelength SCAs are slightly higher than measured in ground testing, which is undoubtedly the result of cosmic-ray hits. The eight short-wavelength SCAs had an average read noise of 6.2 electrons, and the two long-wavelength SCAs had an average of 9.1 electrons in 1000 s in ground testing. In flight, these two values changed to 6.4 and 7.5 electrons, respectively. The long-wavelength SCAs benefit from being surrounded by a colder environment in flight so that the effect of small light leaks in the NIRCam baffles is mitigated.

Because NIRCam generates a large volume of data when all 10 SCAs are read out, a variant of sampling up the ramp is used where two, four, or eight samples are coadded and then a number of reads are clocked but not included in the coadds. Figure 6 illustrates the DEEP8 readout pattern, which can be used for long exposures with all 10 SCAs and still have data volume available for data acquisition in parallel such as imaging with MIRI or NIRISS or spectra with NIRSpec. Other readout patterns with more samples up the ramp can be used when data volume is not a limitation.

Any of the readout patterns with coaddition also include saving the first read separately to recover any pixels that reach saturation in subsequent reads. Currently, the Space Telescope Science Institute pipeline is not using this "Zero read frame" but will do so in the future.

4.2. Wide-field Slitless Spectroscopy

This NIRCam mode uses grisms in NIRCam's long-wavelength arm and is complementary to the NIRISS wide-field slitless mode, which covers 0.8–2.25 μm (Dixon et al. 2015). The NIRCam grisms have $R \sim 1200$, higher than NIRISS grisms, which have $R \sim 150$. NIRCam wide-field slitless spectroscopy (WFSS) works from 2.44 to 4.98 μm. The short-wavelength arms can be used simultaneously with the grisms to acquire a short-wavelength direct image of the field. The zero-deflection wavelength for NIRCam's grisms is 3.94 μm, and sources not in the direct imaging field of view can appear in the grism field of view. This is described in more detail in Greene et al. (2017). Commissioning data updated the spatial locations for best grism coverage as shown in Figure 7. Each module has a pair of grisms with one grism aligned with detector rows and one aligned with detector columns. Taking exposures with each grism can enable better separation of potentially confused sources.

Because the WFSS mode mixes background photons from across the wavelength range with source photons that are dispersed by the grism, this mode is not as sensitive as NIRSpec's slit modes. The NIRCam WFSS mode is ~8 times less sensitive than that of NIRSpec but has the advantage of not requiring preknowledge of source positions. The utility of this mode for observing moderate- to high-redshift galaxies is illustrated in Sun et al. (2022a, 2022b) where WFSS flux calibration data taken during commissioning revealed several $z \sim 6$ galaxies with bright emission lines and little continuum. Figures 8 and 9 show that the grism photon conversion efficiency is higher than prelaunch predictions because there is little or no water or other organic ices on JWST's optical surfaces. The grisms were used to check for ice contamination during commissioning by observing A stars with no ice absorption at 3.1 μm detected. Module A has a higher throughput than Module B because the Module A grisms are antireflection coated on both sides of the grisms while Module B grisms are coated only on the flat side. Only one set of grisms was antireflection coated on the groove side as there was no prior experience demonstrating that coating grooves would not lead to problems. Figure 10 presents the 10σ detection limits in 10,000 s.

During the testing of NIRCam before launch, two types of ghost images were identified in grism data. Figure 11 shows examples of these ghosts. The "tadpole" ghost appears in both Module A and Module B although it is much stronger in Module B (>100×) as a result of the grisms only being antireflection coated on one side. The "tadpole" ghost is mostly seen with Module B column grism and appears at a fixed location relative to the zeroth-order image. The morphology of the tadpole ghost weakly depends on the source position and filter being used. The "shell" ghost has only been seen with Module B so far when very bright sources are observed. Either type of ghost is usually not a concern in module A unless very bright sources are observed.

4.3. Coronagraphy Mode

NIRCam's coronagraphy is based on a standard Lyot-type coronagraph with five focal-plane masks available. The coronagraphic focal-plane masks are not in the imaging field of view unless the pupil wheel is rotated to a Lyot stop with a wedge that deflects the field of view to include the masks. Figure 12 shows the stop used with round masks. The holes are undersized to minimize diffracted light from the edges of the mirror segments. The throughput of the Lyot stops is ~20% so throughput has been traded for better contrast. This optical train is shown schematically in Girard et al. (2022). Figure 13 shows the masks in a flight image against the sky background. There are three round masks sized to match $6\lambda/D$ when combined with F210M (2.1 μm), F335M (3.35 μm), or F430M (4.3 μm). The choice of mask essentially defines the inner working angle. The two bar masks provide more flexibility in terms of choice of wavelength, with the mask widths varying linearly with widths corresponding to $4\lambda/D$ from 1.7 to 2.2 μm or 2.5 to 5 μm. The transmission of the mask substrate drops below 1.7 μm so coronagraphy is not recommended at the shortest wavelengths. The masks are not hard edged but rather Gaussian tapered. Fabrication details are given in Krist et al. (2009). The masks were fabricated at JPL's Microdevices Lab. Girard et al. (2022) present results of coronagraphy tests performed during commissioning, with performance exceeding the expectations given in Perrin et al. (2018) with a firm detection at 3.35 μm of the white dwarf companion HD 114174 B at a separation of $0\farcs5$ and at a contrast of 10 mag (10^4 fainter than the $K \sim 5.3$ host star). One of the first coronagraphic observations after the start of science operations achieved a contrast of better than $10^{-5}(5\sigma)$ at $0\farcs5$ separation using the long-wavelength bar mask at wavelengths from 2.5 to 4.6 μm and as low as 2×10^{-6} at 3 μm and 1″ (Greenabaum 2023). There were no performance requirements defined for the design of the NIRCam coronagraph, but as mentioned above, in-flight performance exceeds preflight simulations in Perrin et al. (2018). As more experience is gained in the use of the coronagraphic mode, performance improvements are likely.

4.4. Time-series Mode

The NIRCam long-wavelength grisms enable transit spectroscopy. In principle, JWST can point at a single target for up to 10 days with only brief breaks to reposition the downlink antenna. This capability is very different from transit work performed using the Hubble Space Telescope (HST), which has to interrupt observations every few tens of minutes unless the target is in the continuous viewing zone. Commissioning transit observations have shown that JWST is a very good platform for observing exoplanet transits

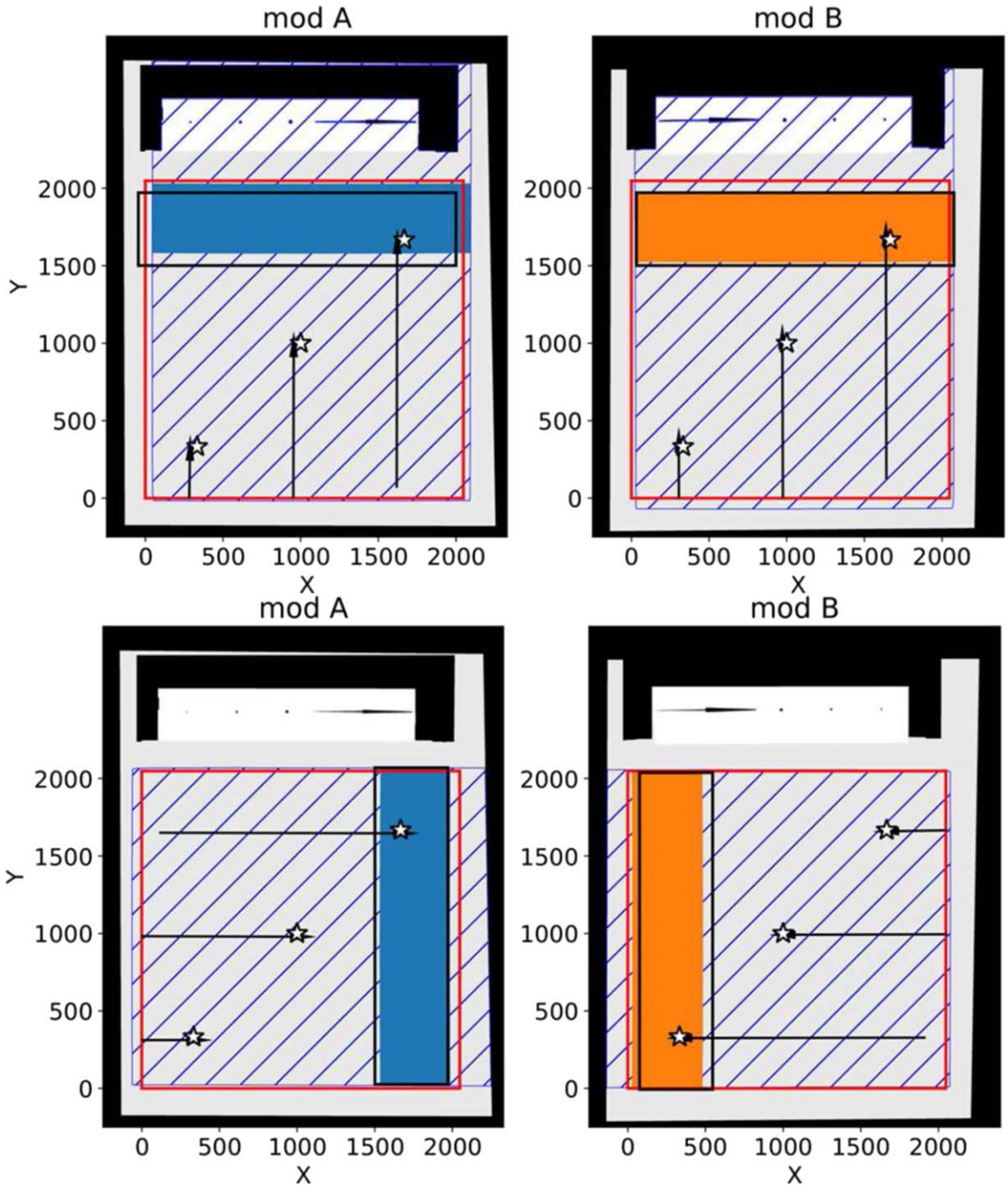

Figure 7. Location of areas for complete grism spectral coverage using F322W2. The upper row shows FOVs for the column grisms, and the lower row displays the row grisms. Diagonal lines indicate the sky area where sources can appear on the detector in grism mode. The red square outlines the detector area. Black rectangles outline the original regions for complete spectral coverage while blue and orange indicate the updated regions for complete spectral coverage. Star symbols illustrate the fraction of the spectral range that is captured for the indicated star locations.

(Schlawin et al. 2023). See Beichman et al. (2014) for an overview of all of JWST's transit capabilities.

One module of NIRCam can be used to study objects where high-time-resolution data are needed. This mode can use any of NIRCam's filters with one choice in the short-wavelength arm and another choice in the long-wavelength arm. The time resolution depends on whether full frame or subarray data are requested. In either readout choice, there is overhead from

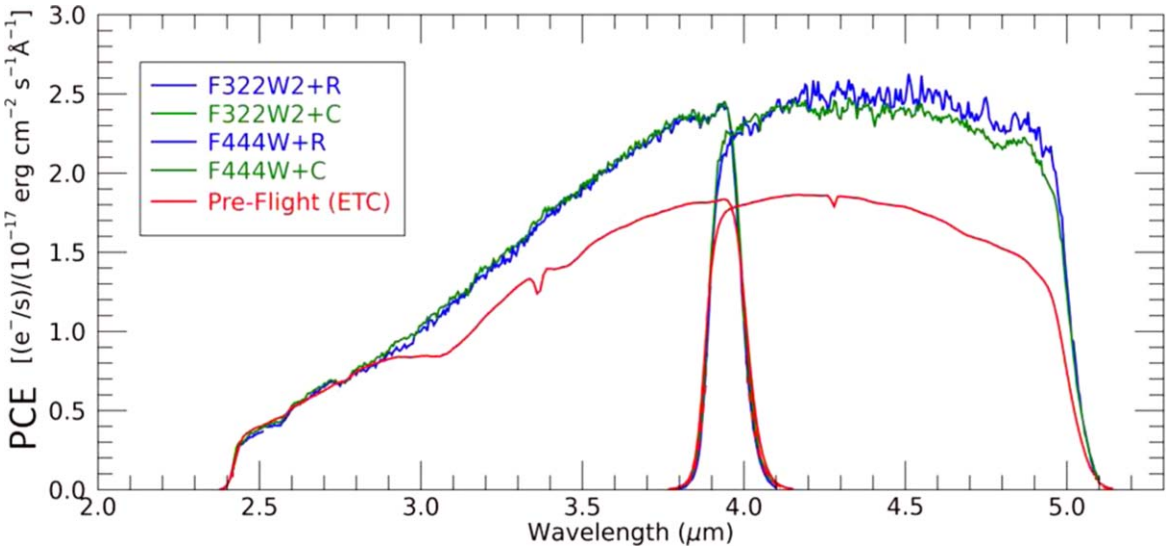

Figure 8. Module A grism photon conversion efficiency derived from observations of P330-E.

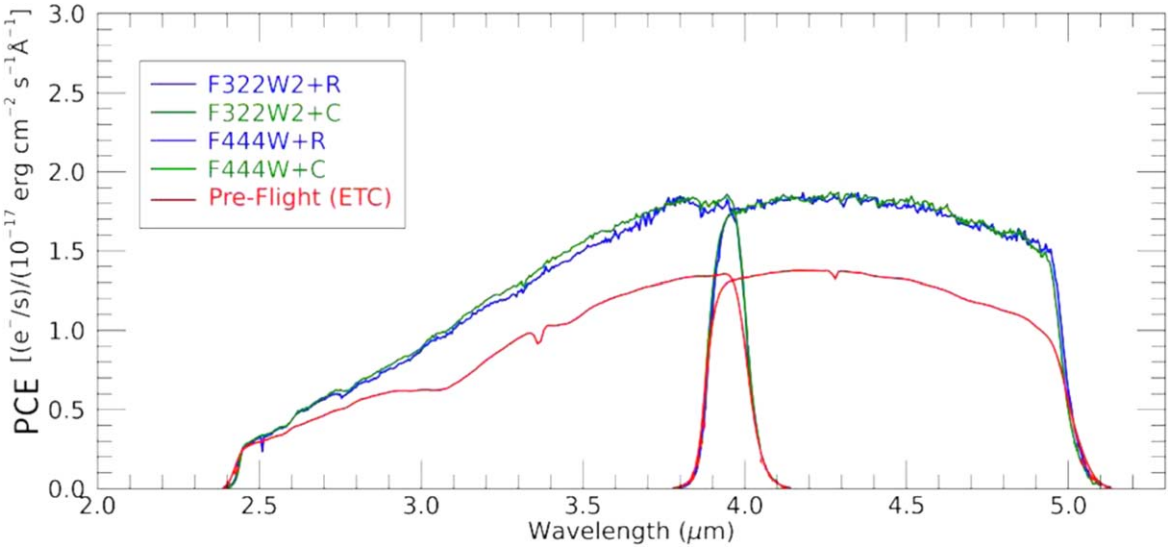

Figure 9. Module B grism photon conversion efficiency derived from observations of P330-E.

resetting the pixels used so in a typical observation, the reset–read–read pattern means in one-third of the time when resetting, no data are collected (this inefficiency is present also for grism time series). The fastest sampling uses a 64 pixel × 64 pixel subarray, which can be read out every 50 ms.

4.4.1. Grism Time Series

NIRCam's grism time-series capability was successfully demonstrated during commissioning. The current implementation of this mode uses a weak lens in the short-wavelength arm and a grism with $R \sim 1500$ band-limited with either the F277W, F322W2, F356W, or the F444W filter in the long-wavelength arm. The grism time-series mode only uses Module A. The sensitivity curve in Figure 8 is relevant also for this mode and shows that the F322W2 spectral range is 2.4 to 4 μm and is 3.9 to 5.0 μm for F444W. This mode can take advantage of the "stripe" mode where the SCA is read out using all four output amplifiers present in the SCA but only enough rows to capture the grism spectrum. This scheme uses the row grism only. The shortest readout time is provided by using a 64 × 2048. This enables observing significantly brighter stars

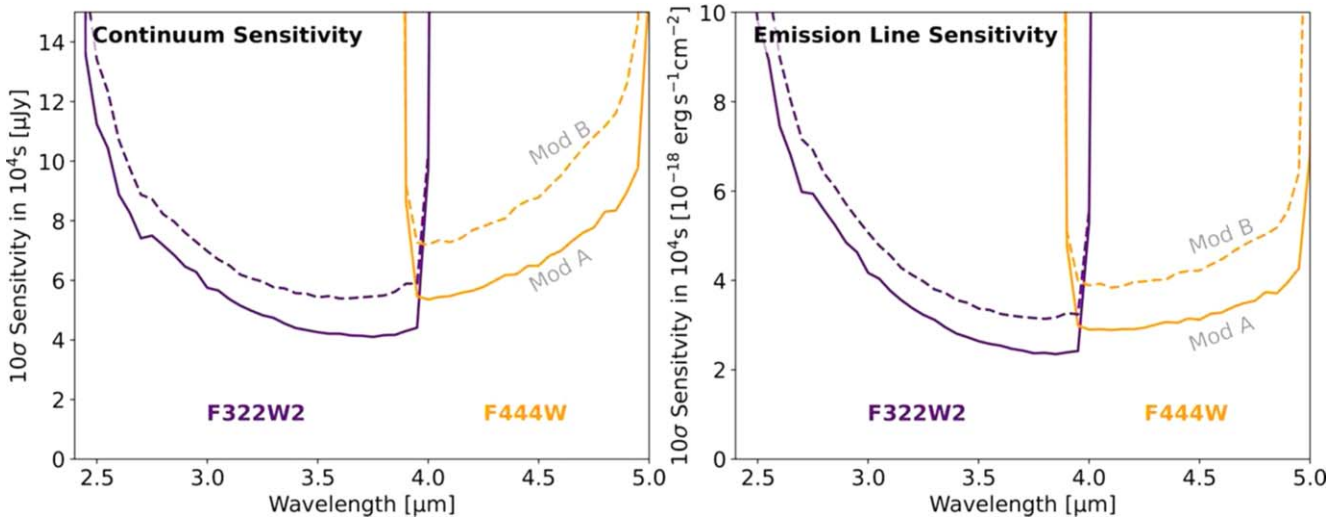

Figure 10. Module A grism continuum and line sensitivities for a 10σ detection in 10,000 s.

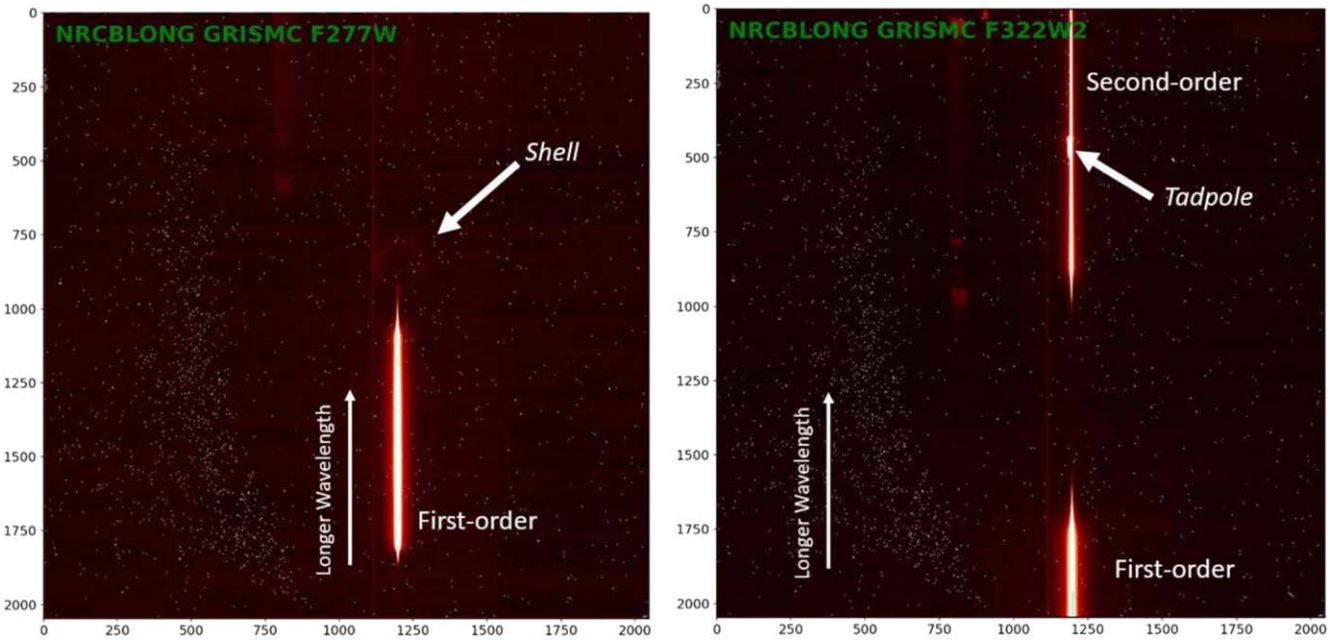

Figure 11. On the left, the "shell" grism ghost. The mechanism for this ghost was never definitively determined but likely involves multiple reflections between the grism, filter, and camera lens(es). On the right, a "tadpole" ghost is seen and is likely the zeroth-order grism image reflected off the filter, back to the grism, and then appearing as a zeroth-order image on the detector. "Tadpoles" appears at a fixed location relative to an object's zeroth-order image.

than the usual subarray mode, which reads out using only one of the SCA output amplifiers. Table 3 gives the Vega magnitudes at $K(2.2\,\mu\mathrm{m})$ for several wavelengths in the spectrum using either F322W2 or F444W. The table assumes that the data are taken using a reset followed by clocking through pixels to read the pixel charge followed by a second read (RAPID mode with two groups). Using a reset followed by a single read could make the saturation limit 0.75 mag brighter at the expense of the readout noise being increased by the kTC noise of ~35 electrons.

Several important lessons from commissioning indicate that this mode may be more user friendly than the modes used for transit observations on the HST. First, the time for detectors to settle after the start of time-series observation is nearly instantaneous with a timescale of less than 4 minutes to stabilize to a level of less than 150 ppm variation (Schlawin

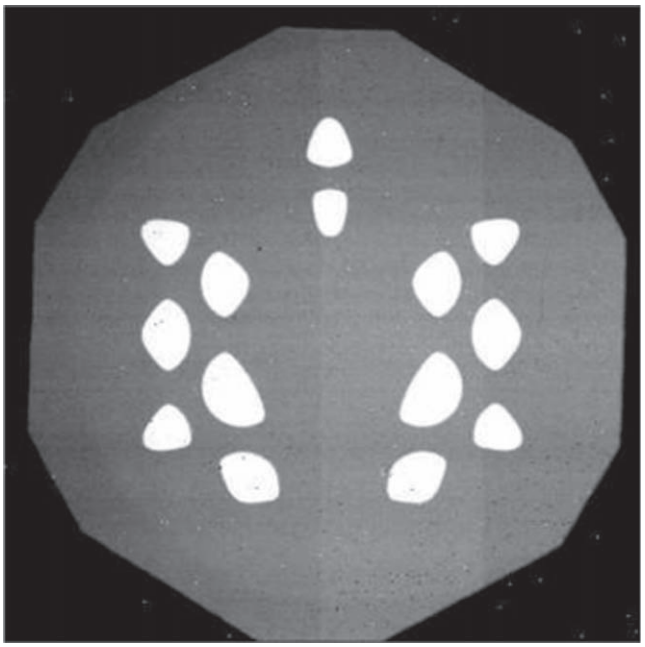

Figure 12. An image of the Lyot stop used with round focal-plane masks taken using the pupil imaging lens.

et al. 2023) rather than the few tens of minutes required by WFC3IR detectors. Second, the data analysis is more straightforward than for Hubble transit data. The noise performance for a region of less than 30 pixels is at the expected level for photon-limited statistics. The broadband light curve averages down as $1/\sqrt{N}$ to ~20 ppm after correction for a downward trend in the signal level. Section 5 describes an enhancement to this mode where the short-wavelength arm could use the 0° DHS to acquire spectra in the 1–2 μm region simultaneously with the grism spectrum.

4.5. In-flight Anomalies

4.5.1. Cosmic Rays

Cosmic rays are an expected annoyance for space instrumentation. Figure 14 shows a ramp from a pixel with a large cosmic-ray hit that saturated the pixel between reads three and four. The last reads show a slight decrease in charge as the charge migrates to adjacent pixels. Most hits like the one shown here affect only one pixel and rarely a short streak of pixels. The pipeline takes these hits into account and only uses good data to derive a signal. The pipeline inserts a flag in the data quality plane in the FITS file for an image to indicate that a cosmic-ray hit was detected in a given pixel. The rate of hits matches the prelaunch estimates.

What caught some by surprise was the detection of "snowballs" as shown in Figure 15. The snowballs have appreciable spatial extent, with some affecting as many as 100 pixels. Typically, many of these pixels receive a saturating level of charge as illustrated in the surface plot in Figure 15. Similar events had been seen in earlier space missions using HgCdTe detectors, but because the rate is quite low, they were rarely seen. Webb has a much larger number of 2K × 2K arrays so these events are more noticeable. Approximately 170 events per hour per array are seen in NIRCam arrays with roughly similar rates observed in NIRSpec and NIRISS. There is no definitive explanation for these events. HgCdTe arrays are comprised of higher atomic weight materials than CCDs, and this suggests that a cosmic ray could hit a heavy-element nucleus and create energetic high-atomic-number nuclei by spallation, which then deposit significant charge in a set of pixels (G. Rieke 2023, private communication).

Table 3
Vega K Magnitude for Stars Reaching 80% of the Full Well Using the Stripe Mode and Reset–Read–Read

Filter	λ (μm)	K_{mag}
F322W2	2.40	3.99
F322W2	2.75	4.37
F322W2	3.23	4.10
F322W2	4.00	3.90
F444W	3.90	3.96
F444W	4.41	3.33
F444W	5.00	1.99

4.5.2. Persistence

Three of NIRCam's SCAs, NRCA3, NRCB3, and NRCB4, exhibit noticeable persistence even several thousands of seconds after illumination as shown in Figure 16. A typical time between the end of one program and the start of the next is ~1800 s, so scheduling very bright source observations immediately prior to programs with long, low-signal observations should be avoided. Saturating cosmic-ray hits, and snowballs in particular, can result in persistence images of the hit.

4.5.3. Scattered Light and Glints

Occasional glints were expected from ground tests, but some glints and some scattered-light features were a surprise. The scattered-light features are described in Rigby et al. (2023) and are caused by sneak paths through the aft optics baffle and by scattering off reflective material on the upper secondary mirror support strut. During ground tests, glints (sometimes called "Dragon's Breath") were discovered. Similar artifacts have been observed in HST instruments and result from relatively bright point-source scattering and diffracting off sharp edges. A commissioning test collected images with a star moved across the edges of the focal-plane masks on the focal-plane assemblies. Figure 17 shows a typical glint coming off a sharp

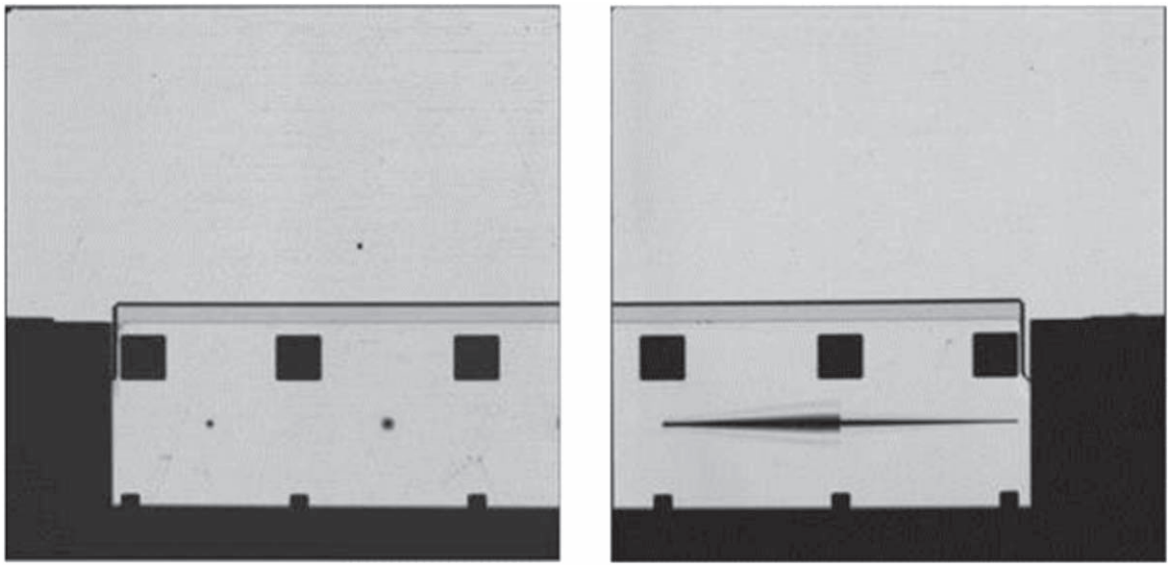

Figure 13. View of Module A's masks through the short-wavelength channel. The squares along the edge of the field are neutral density spots used for target acquisition.

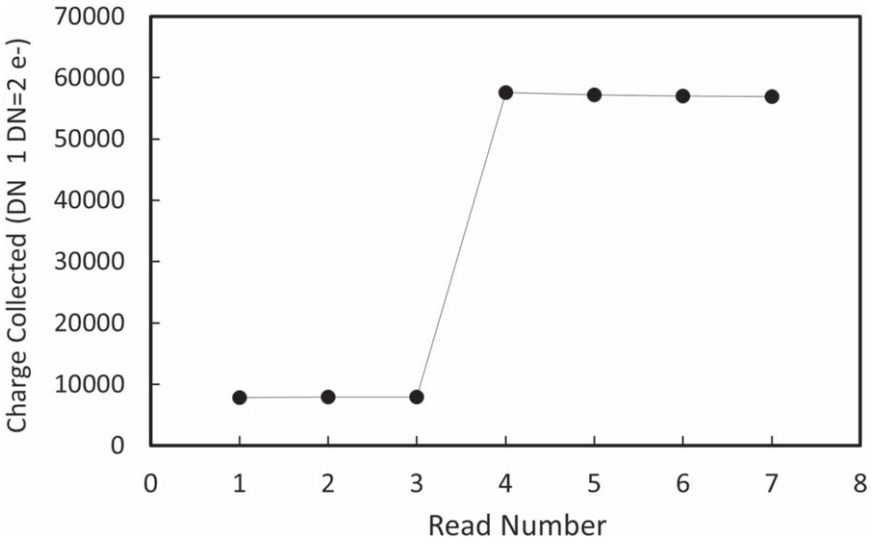

Figure 14. Ramp from a pixel hit by a cosmic-ray.

edge in the focal-plane mask and is similar to those seen in the ground test. Another type of glint is shown in Figure 18 where light glances off a sharp edge inside the NIRCam focal-plane housing.

5. Future Improvements

Several enhancements to the modes described in Section 4 will improve observing efficiencies. These include using the DHS in parallel with the long-wavelength grism for time-series observations and improving coronagraphy to permit simultaneous short- and long-wavelength coronagraphy. Combining DHS observations with grism observations yields simultaneous wavelength coverage from 1.0 to 2.0 μm and either 2.4 to 4.0 μm or 3.9 to 5 μm depending on the choice of long-wavelength filter (Schlawin et al. 2017; see DHS + grism data sample in this paper). This mode would not provide the continuous 1–5 μm coverage afforded by NIRSpec but would provide some short-wavelength spectral coverage on bright ($J < 11$) sources that saturate in NIRSpec's prism mode. The NIRISS Single Object Slitess Spectroscopy mode would provide

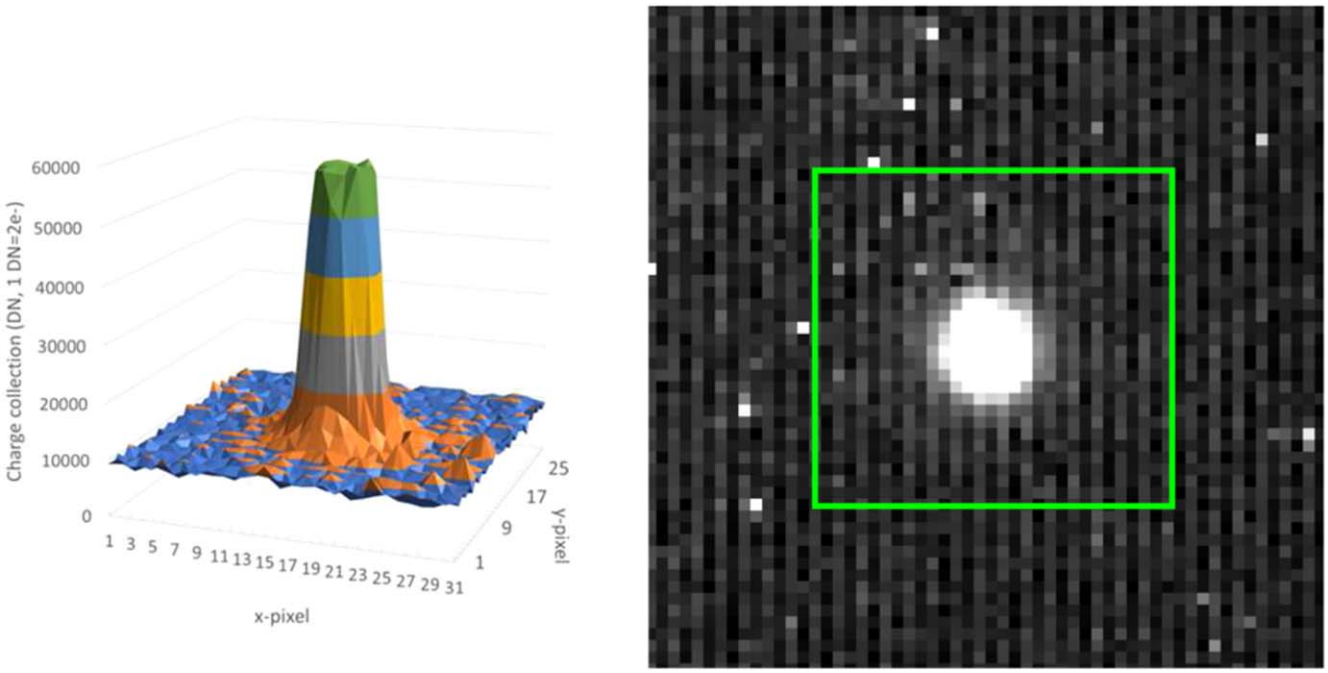

Figure 15. The right-hand image shows a snowball as seen in a single frame on a ramp. The green box outlines the region shown in the surface plot at left.

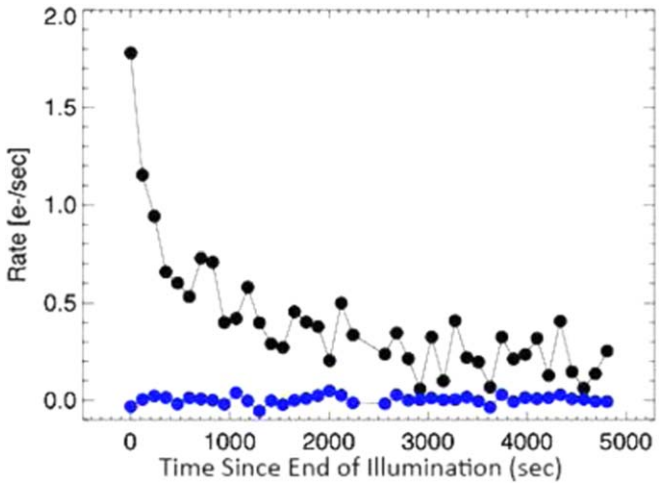

Figure 16. Persistence seen in NRCA3. The blue points are from a dark exposure while the black points are the brightest pixel in a dark taken immediately after an on-sky image.

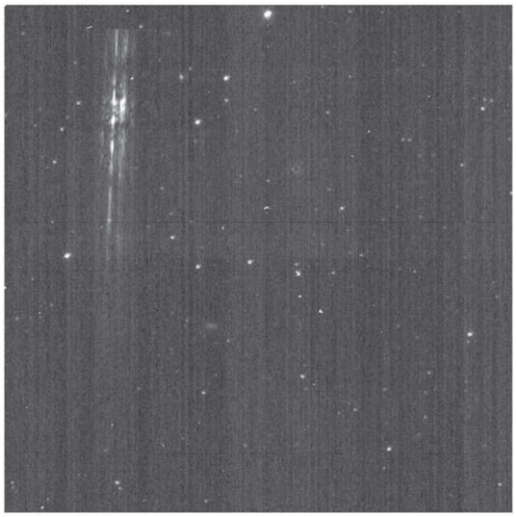

Figure 17. An example of a glint caused by starlight scattering off a sharp edge in the focal-plane mask.

more complete coverage for $\lambda < 2.5$ μm but does not provide any longer-wavelength coverage. Schlawin et al. (2017) describe the benefits for molecular abundance retrievals using this NIRCam mode.

Acquisition of simultaneous short-wavelength and long-wavelength coronagraphy would use a long-wavelength coronagraphic mask such as MASK335R. At 0.″5 separation, this mask would provide good contrast, similar to the $\sim 10^{-5}$ already achieved in the long-wavelength arm and better than the contrast of 5×10^{-5} achieved at 2.1 μm using MASK210R (Girard et al. 2022). These contrasts would come at the expense of loss of some inner working angle at short wavelengths compared to using MASK210R. However, for some observations such as studying debris disks, the loss of some area in the short-wavelength image is far outweighed by the time savings of observing two wavelengths at once.

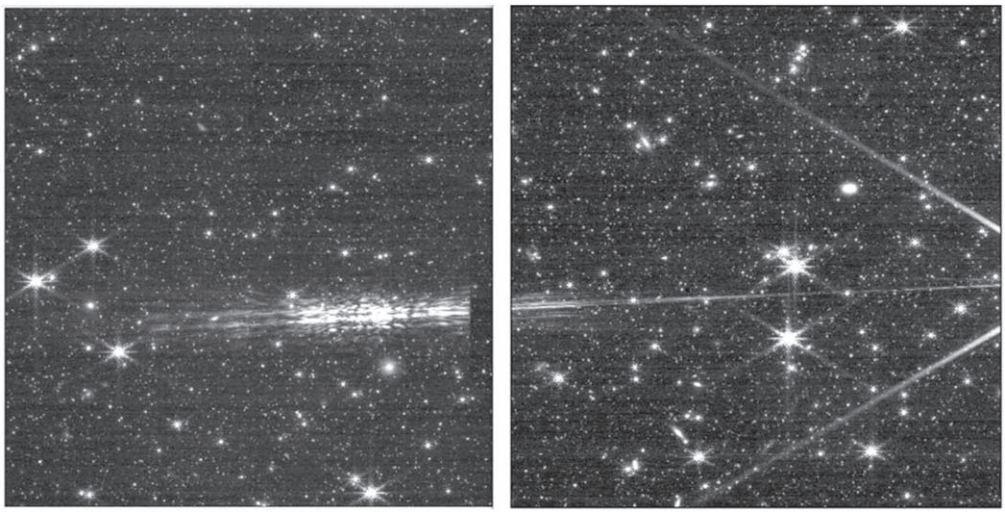

Figure 18. An example of a glint caused by starlight scattering off a sharp edge inside the focal-plane housing. Adjacent short-wavelength SCAs are shown with the glint from a single star extending across both.

Simultaneous short- and long-wavelength coronagraphy will be available to Cycle 2 proposers, and DHS transit use will be available in the future.

NIRCam and JWST have been demonstrated to work very well and have enabled exciting observations as revealed by several Early Release Observations and Early Science Observations.

Many people at Lockheed Martin's Advanced Technology Center contributed to the NIRCam Project. We especially want to thank Alison Nordt, Eric Dixon, Tony Magoncelli, and Liz Osborne for support during commissioning. The development, testing, and commissioning of NIRCam were funded by NASA Contract NAS5-02105. A portion of this research was carried out at the Jet Propulsion Laboratory, California Institute of Technology, under a contract with the National Aeronautics and Space Administration (80NM0018D0004). D.J. is supported by NRC Canada and by an NSERC Discovery Grant. We also want to acknowledge the contributions of three NIRCam team members who passed away during the development of NIRCam. Chad Engelbracht analyzed much of the detector test data that were used to select the flight parts. John Stauffer devised the original calibration plan for NIRCam. Don Hall provided advice on many issues and detector production in particular. The referee is thanked for helpful suggestions.

ORCID iDs

Marcia J. Rieke https://orcid.org/0000-0002-7893-6170
Thomas P. Greene https://orcid.org/0000-0002-8963-8056
Kevin Hainline https://orcid.org/0000-0003-4565-8239
Jarron Leisenring https://orcid.org/0000-0002-0834-6140
Everett Schlawin https://orcid.org/0000-0001-8291-6490
Fengwu Sun https://orcid.org/0000-0002-4622-6617
Christopher N. A. Willmer https://orcid.org/0000-0001-9262-9997
Anton M. Koekemoer https://orcid.org/0000-0002-6610-2048
Armin Rest https://orcid.org/0000-0002-4410-5387
Charles Beichman https://orcid.org/0000-0002-5627-5471
Daniel J. Eisenstein https://orcid.org/0000-0002-2929-3121
Klaus Hodapp https://orcid.org/0000-0003-0786-2140
George H. Rieke https://orcid.org/0000-0003-2303-6519

References

Acton, D. S., Atcheson, P. D., Cermak, M., et al. 2004, Proc. SPIE, 5487, 887A
Acton, D. S., Knight, J. S., Chonis, T., et al. 2018, Proc. SPIE, 10698, 106983P
Acton, D. S., Knight, J. S., Contos, A., et al. 2012, Proc. SPIE, 8442, 84422H
Acton, D. S., Knight, S., Carrasquilla, M., et al. 2022, Proc. SPIE, 12180, 121800U
Beichman, C. A., Benneke, B., Knutson, H., et al. 2014, PASP, 126, 1134
Dixon, W., Ravindranath, S., & Willott, C. 2015, Proc. IAU, 319, 11
Girard, J. H., Leisenring, J., Kammerer, J., et al. 2022, Proc. SPIE, 12180, 121803Q
Greenabaum, A. 2023, arXiv:2301.11455
Greene, T. P., Kelly, D. M., Stansberry, J., et al. 2017, JATIS, 3, 035001
Huff, L. W. 2005, Proc. SPIE, 5904, 30
Krist, J. E., Balasubramanian, K., Beichman, C. A., et al. 2009, Proc. SPIE, 7440, 74400W
Perrin, M., Acton, D. S., Lajoie, C.-P., et al. 2016, Proc. SPIE, 9904, 99040F
Perrin, M. D., Pueyo, L., Van Gorkom, K., et al. 2018, Proc. SPIE, 10698, 1069809
Plazas, A., Shapiro, C., Smith, R., Rhodes, J., & Huff, E. 2017, JInst, 12, C04009
Rigby, J., Perrin, M., McElwain, M., et al. 2023, PASP, in press
Schlawin, E., Beatty, T., Brooks, B., et al. 2023, PASP, 135, 1043
Schlawin, E., Rieke, M., Leisenring, J., et al. 2017, PASP, 129, 015001
Stockman, H. S. 1997, The Next Generation Space Telescope: Visiting a Time when Galaxies were Young (Washington, DC: AURA)
Sun, F., Egami, E., Pirzkal, N., et al. 2022a, ApJL, 936, L8
Sun, F., Egami, E., Pirzkal, N., et al. 2022b, arXiv:2209.03374